

Customizable gradient MXene/polyurethane modules for electromagnetic interference shielding with low reflection and thermal management

Yuhui Feng^a, Mingye Zhu^a, Wenjun He^a, Yan Bai^a, Ning Ding^a, Zhen You^a, Xiang Zou^a, Weiwei Zhao^a, Shujuan Liu^{a,*}, Qiang Zhao^{a,b,*}

^a State Key Laboratory of Organic Electronics and Information Displays & Jiangsu Key Laboratory for Biosensors, Institute of Advanced Materials (IAM), Nanjing University of Posts & Telecommunications, 9 Wenyuan Road, Nanjing 210023, P. R. China

^b College of Electronic and Optical Engineering & College of Flexible Electronics (Future Technology), Nanjing University of Posts & Telecommunications, 9 Wenyuan Road, Nanjing 210023, P. R. China

ARTICLE INFO

Keywords:

Customizable gradient structure
MXene
Low reflection
Electromagnetic interference shielding
Thermal management

ABSTRACT

The conductive polymer composites (CPC) with elevated levels of conductivity typically exhibit enhanced electromagnetic interference shielding effectiveness (EMI SE), however, this enhancement is often paralleled by an augmented risk of secondary electromagnetic (EM) pollution, attributable to the increased EM reflection. Developing a facile method to construct an eco-friendly CPC for EMI shielding that simultaneously exhibits low reflection and high shielding performance remains a promising yet challenging pursuit. Moreover, excellent shielding materials should possess exceptional thermal management capabilities to protect individuals or equipment under extreme conditions. Herein, we have engineered the MXene/polyurethane (MXene/PU) sponge (MPS) modules characterized by the hierarchical porous structure. Through the strategic modular combination of impedance-matching and impedance-mismatching modules tailored for different application contexts, the customizable gradient MXene/PU sponge (GMPS) facilitates achieving a balance of exceptional average EMI SE (44.6 dB), a low reflection coefficient ($R = 0.18$), and superior photo/electrothermal conversion capability. Furthermore, both experimental results and finite element analyses are adopted to explore the effect of the arrangement order of GMPS on EMI shielding performance. Leveraging the green, health-conscious, and flexibly customizable approach, it manifests tremendous potential across various areas, including intelligent residences and multifunctional integrated systems.

1. Introduction

With the rapid development of the Internet of Things (IoT), the widespread utilization of portable/wearable electronic devices has brought significant convenience. Nonetheless, signal radiation-induced electromagnetic interference (EMI) may cause substantial damage to precision electronic equipment, while sustained exposure to electromagnetic waves (EMWs) raises health concerns, especially for vulnerable groups such as pregnant women, infants, and patients [1–3]. In response to the hazard posed by electromagnetic radiation (EMR), the development of novel materials that are both lightweight and flexible, yet exhibit high shielding effectiveness (SE) for EMI shielding, has become an important research area. Meanwhile, emerging EMI shielding materials are being engineered with advanced thermal management

properties, crucial for maintaining optimal temperatures in wearable devices and ensuring accurate functioning of instruments during outdoor operations [4–6]. Currently, ultralight conductive polymer composites (CPC) are rapidly developed as EMI shielding materials benefiting from their easy processing and distinctive three-dimensional (3D) porous conductive networks [7–9]. Simultaneously, two-dimensional (2D) transition metal carbides and/or nitrides Ti_3C_2Tx (MXene) have attracted attention in the field of EMI shielding and electro/photo-thermal conversion as the nanofiller of CPC due to their unique layered structure, abundant functional groups, excellent conductivity, and local surface plasmon resonance (LSPR) characteristics [10–12]. However, MXene-based CPC with a homogeneous high-conductive network exhibit high reflection of EMWs into free space due to impedance mismatching between the material surface and air,

* Corresponding authors at: State Key Laboratory of Organic Electronics and Information Displays & Jiangsu Key Laboratory for Biosensors, Institute of Advanced Materials (IAM), Nanjing University of Posts & Telecommunications, 9 Wenyuan Road, Nanjing 210023, P. R. China.

E-mail addresses: iamsjliu@njupt.edu.cn (S. Liu), iamqzhao@njupt.edu.cn (Q. Zhao).

leading to serious secondary EMR contamination [13,14]. To minimize the secondary EMR pollution, absorption-dominated EMI shielding CPC with low reflection is greatly desired for various life scenarios. It is well-established that the attenuation of dielectric properties in EMI shielding materials could lead to a reduction in EW wave reflection, however, this modification often reduces the EMI SE and energy conversion potential due to weak absorption losses and limited Joule heating within the material [15]. Therefore, a further understanding of the structure and function of MXene-based CPC EMI shielding material is critical for the design and development of advanced EMI shielding materials with low electromagnetic (EM) reflection under high EMI shielding performance and excellent thermal management capability [16,17].

Through designing and constructing asymmetric gradient structures, the layers closest to the incident EMWs exhibit optimal impedance matching, thereby diminishing EM reflection and facilitating deeper penetration of EMWs into the composite for enhanced absorption [16]. At present, the establishment of common gradient structures includes three types: structural gradient, concentration gradient, and component gradient. Structural gradient refers to the formation of a gradient structure based on size within a single-component nanomaterial sample [18–20]. For instance, Kim et al. demonstrated a monotonic gradient impedance-graded structure via the size-selective sedimentation of aluminum nanoflakes in a dispersion, which delivered a total shielding effectiveness (SE_T) value of 26.80 dB and a reflection shielding

effectiveness (SE_R) value of 0.04 dB across the frequency range of 1.5–10 GHz [21]. Analogous to structural gradients, concentration gradients emerge within single-component constructs. Xue et al. reported a gradient-conductive structure obtained by continuous 3D printing of MXene/carbon nanotubes (CNT)/poly (amic acid) inks with different CNT contents, which performs a low reflection coefficient ($R = 0.23$) [15]. In contrast to symmetric materials characterized by uniform fillers or structures, the fabrication of a gradient structure can markedly attenuate EM reflection while maintaining a comparable SE value, even with a consistent total filler content [22–24]. For high-dielectric EMI shielding materials, the incorporation of magnetic fillers or additional dielectric constituents can significantly improve impedance matching. The strategic assembly of multilayered structures, which feature gradients of electric/magnetic or electric/electric conductive layers, also establishes optimal conditions for the attenuation of EM reflection [25–29]. In addition, there are still many situations where multiple gradient modes work together. Yang et al. prepared gradient filler distributions with nickel-coated carbon fiber and introduced magnetic ferric oxide-supported carbon nanotubes to reduce secondary EMWs pollution [30–33]. In general, enhancing the impedance matching between the EMI shields and air through the elaborate design of various gradient structures is critical in diminishing the reflection of EMWs at the interface.

While the construction of asymmetric gradient structures facilitates

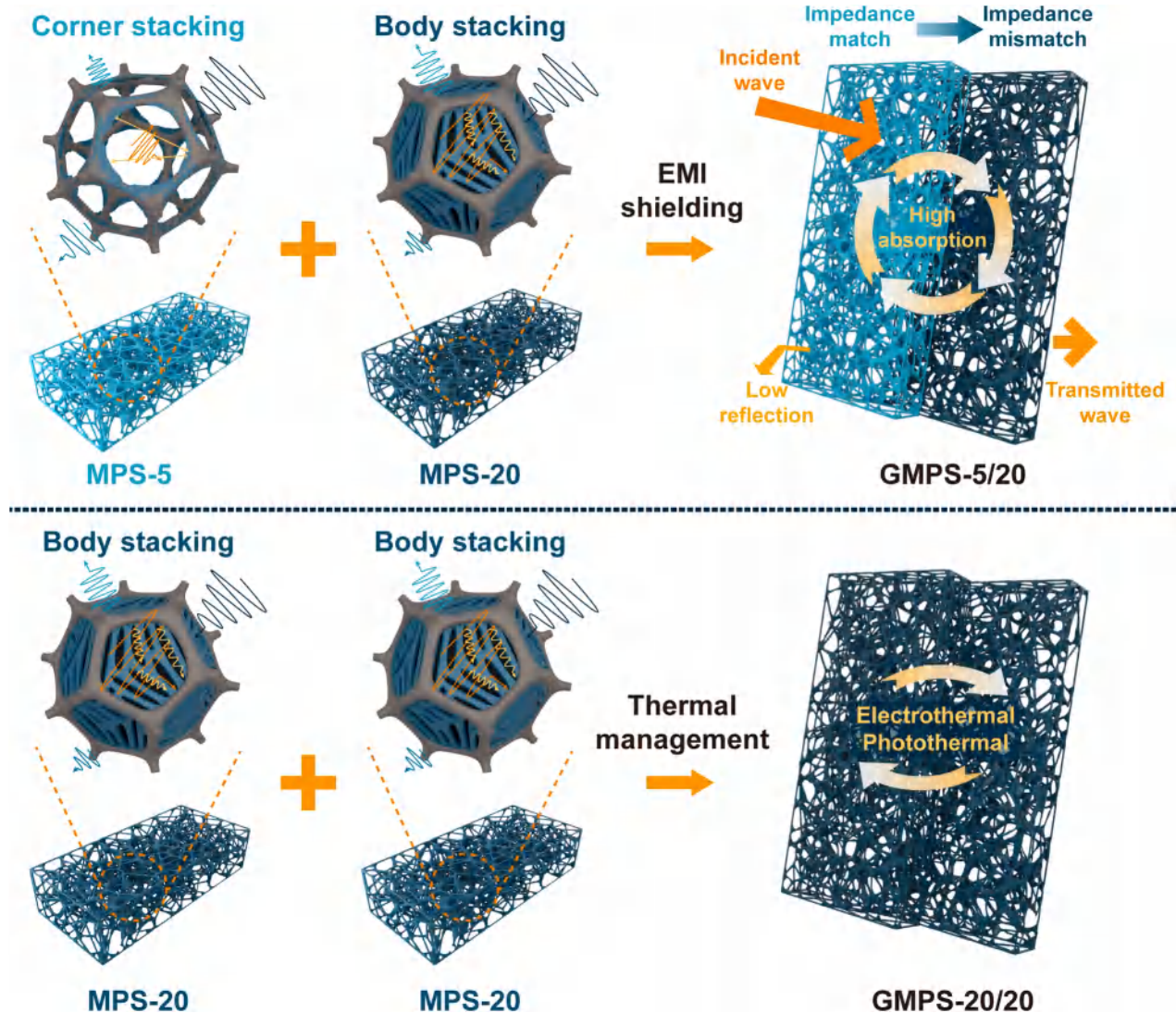


Fig. 1. Customizable gradient modular design and assembly of GMPS with low reflection and thermal management and its EMI shielding mechanism.

the modulation of EMI shielding performance and the reduction of secondary EMWs reflections, the complexity of this process restricts its flexibility, thereby constraining its broader application. Herein, we report a customizable modular solution to fabricate gradient MXene polyurethane (PU) sponge (GMPS) modules through the arbitrary combination with MXene PU sponge (MPS) modular units. Fig. 1 shows the customizable gradient modular design and assembly of GMPS with low reflection and thermal management and its EMI shielding mechanism. In GMPS, the slightly conductive module (impedance-matching layer) of MPS serves as the EM absorption unit to reduce the secondary reflected EMWs. On the contrary, the highly conductive module (impedance-mismatching layer) of MPS acts as an EM reflection unit to enhance the EMI shielding performance. Both of them form an absorption-reflection-reabsorption path. Attributed to the synergistic effect of hierarchical porous structure and MXene intrinsic properties, the customizable GMPS modules exhibit a wide EMI SE tuning range of 44.6–56.2 dB as well as a wide R tuning range of 0.61–0.18. To explore the influences of asymmetric gradient structures on the EMI shielding performance, the electric field norm and power flow were calculated by finite element analyses (FEA). Simultaneously, the GMPS modules demonstrate an excellent electrothermal and photothermal conversion effect. To simulate practical applications, large-sized samples were prepared for use as wallpaper and heater, successfully achieving EMI shielding and thermal management functions. This work provides a novel strategy for designing EMI shielding materials with low EMWs reflection and excellent capability of energy conversion, which has great potential in the fields of flexible electronic devices, advanced thermal management, and multifunctional integrated systems.

2. Experimental section

2.1. Materials

The 99.99% purity 400-mesh Ti_3AlC_2 powders were provided by Jilin 11 Technology Co., Ltd (Jilin, China). Hydrochloric acid (HCl) was obtained from Nanjing Chemical Reagent Co., Ltd (Nanjing, China). Lithium fluoride (LiF) was acquired by Shanghai Aladdin Biochemical Technology Co., Ltd (Shanghai, China). Absolute ethanol (C_2H_6O) was a commercial material from Wuxi Yasheng Chemical Co., Ltd (Wuxi, China). Deionized water was produced in the laboratory. Commercial polyurethane sponges were purchased from Alibaba (China) Co., Ltd (Hangzhou, China).

2.2. Characterization

X-ray diffraction (XRD) patterns were measured using an X-ray diffractometer (D8 Advance A25, Bruker) with $Cu K\alpha$ radiation ($\lambda = 1.5418 \text{ \AA}$) in the range from 5 to 65° . Scanning electron microscopy (SEM) images were characterized using a field emission scanning electron microscope (S-4800, Hitachi, 5 kV), and transmission electron microscopy (TEM) images were measured using a transmission electron microscope (HT7700, Hitachi, 200 kV). The Fourier transform infrared (FT-IR) spectra were measured by a Fourier transform infrared spectrometer (Spectrum Two, PerkinElmer). The compressive mechanical properties of the composites were evaluated using the motorized force tester (ESM303, Mark-10) at room temperature with a speed of 20 mm/min. The ultraviolet-visible-near infrared (UV-vis-NIR) absorption spectra were recorded using a spectrophotometer (UV-3600, Shimadzu) with a scanning range from 350 to 870 nm. The conductivity of the MPS was measured using the four-probe tester (ST2263, Suzhou Jingge Electronics Co., Ltd.). The EMI SE of the MPS and GMPS was measured by a rectangular waveguide (WR-90) using a 2-port network analyzer (ENA5071C, Agilent Technologies) at the frequency range of 8.2–12.4 GHz. The EMI shielding test was detailedly described in the [Supplementary Information](#). During the photothermal and electrothermal conversion tests, the real-time temperature variation of the materials

was measured and documented using an infrared thermal imaging camera (E40, Teledyne FLIR). The 808 nm laser light source (MW-GX-808/1–5000 mW cm^{-2}) was connected to an optical shutter through a multimode fiber, and the shutter was coupled to a plastic optical fiber. The light intensity can be observed via a laser power meter (VLP-2000-2 W). The Joule heating performance was assessed by connecting the GMPS to an electrochemical workstation (CHI 660E, CHENHUA).

2.3. Synthesis of $Ti_3C_2T_x$ MXene colloidal dispersion

The colloidal dispersion of MXene was prepared by etching the Al layer from Ti_3AlC_2 powder with HF acid as the etchant solution and subsequent mechanical delamination, following the previously reported methods [34]. Firstly, LiF (0.5 g) was dissolved in HCl (10 mL, 9 M). Then the Ti_3AlC_2 powder (0.5 g) was slowly added to the above mixture and heated at 60°C for 24 h. Secondly, the reacted product was washed using deionized water via centrifugation several times until the pH exceeded 6. Then, the product was dried under vacuum for 12 h. Next, the multilayer $Ti_3C_2T_x$ product (50, 100, 150, and 200 mg) was dispersed in deionized water (10 mL), respectively, and sonicated under Ar for 1 h. Finally, the $Ti_3C_2T_x$ nanosheets supernatant was collected through centrifugation at 3500 rpm for 1 h.

2.4. Fabrication of MPS and GMPS

The non-gradient MPS was fabricated through dip-coating and freeze-drying processes. Firstly, the 50 ppi PU sponge (“ppi” represents the average pore size of the PU sponge, defined by the number of pores per inch; 50 ppi pore size $\approx 1100 \mu\text{m}$) was cut into the desired size (22.86 mm \times 10.16 mm, 3 mm in thickness) and washed ultrasonically several times with ethanol (50%), followed by a complete drying process in the vacuum oven at 60°C for 2 h [35]. Then, the obtained PU sponge was dipped into 2 mL $Ti_3C_2T_x$ nanosheets solutions (5, 10, 15, and 20 mg mL^{-1}) through multiple extrusions, quickly frozen at -70°C , and lyophilized in a freeze dryer at -40°C for 24 h. After the dip-coating and freeze-drying processes, the $Ti_3C_2T_x$ nanosheets were deposited onto the surface of the sponge skeleton, forming the MPS with a 3D porous network structure. The gradient-conductive GMPS frame was obtained by superimposing two MPS prepared from $Ti_3C_2T_x$ nanosheets solutions with the same or different concentrations. Following the customizable modular strategy tailored for different application contexts, there were no additional adhesives present between the adjacent interfaces of two MPS.

3. Results and discussion

3.1. Design and characterization of MPS and GMPS

The fabrication of ultrathin $Ti_3C_2T_x$ MXene nanosheets is shown in Fig. S1. Firstly, SEM images display that the Ti_3AlC_2 MAX precursor was etched through the HCl and LiF mixture to remove Al atomic layers, and the “accordion” structure multilayer $Ti_3C_2T_x$ (m- $Ti_3C_2T_x$) was generated (Fig. S2a,b) [10,36,37]. The XRD patterns in Fig. S2c show that the most intense peak at $2\theta \approx 39^\circ$ of Ti_3AlC_2 MAX disappeared, which revealed the removal of Al atomic layers and the formation of m- $Ti_3C_2T_x$. Meanwhile, the (002) characteristic peak shifted to a lower angle, indicating the expansion of the interlayer spacing in m- $Ti_3C_2T_x$ [36,38]. Then, through sonication and centrifugation of the m- $Ti_3C_2T_x$ solution, the aqueous dispersion composed of delaminated MXene nanosheets was prepared, and the colloidal dispersibility of MXene nanosheets dispersion could be confirmed by the observation of the Tyndall scattering effect (Fig. S3) [39]. TEM image displays that MXene nanosheets were single-layer flakes with an average diameter of 400 nm (Fig. S2d).

Fig. 2a illustrates a schematic of the MPS sample prepared by a simple dip-coating and freeze-drying process. To obtain MXene-based porous architectures efficiently, the commercial PU sponge with the

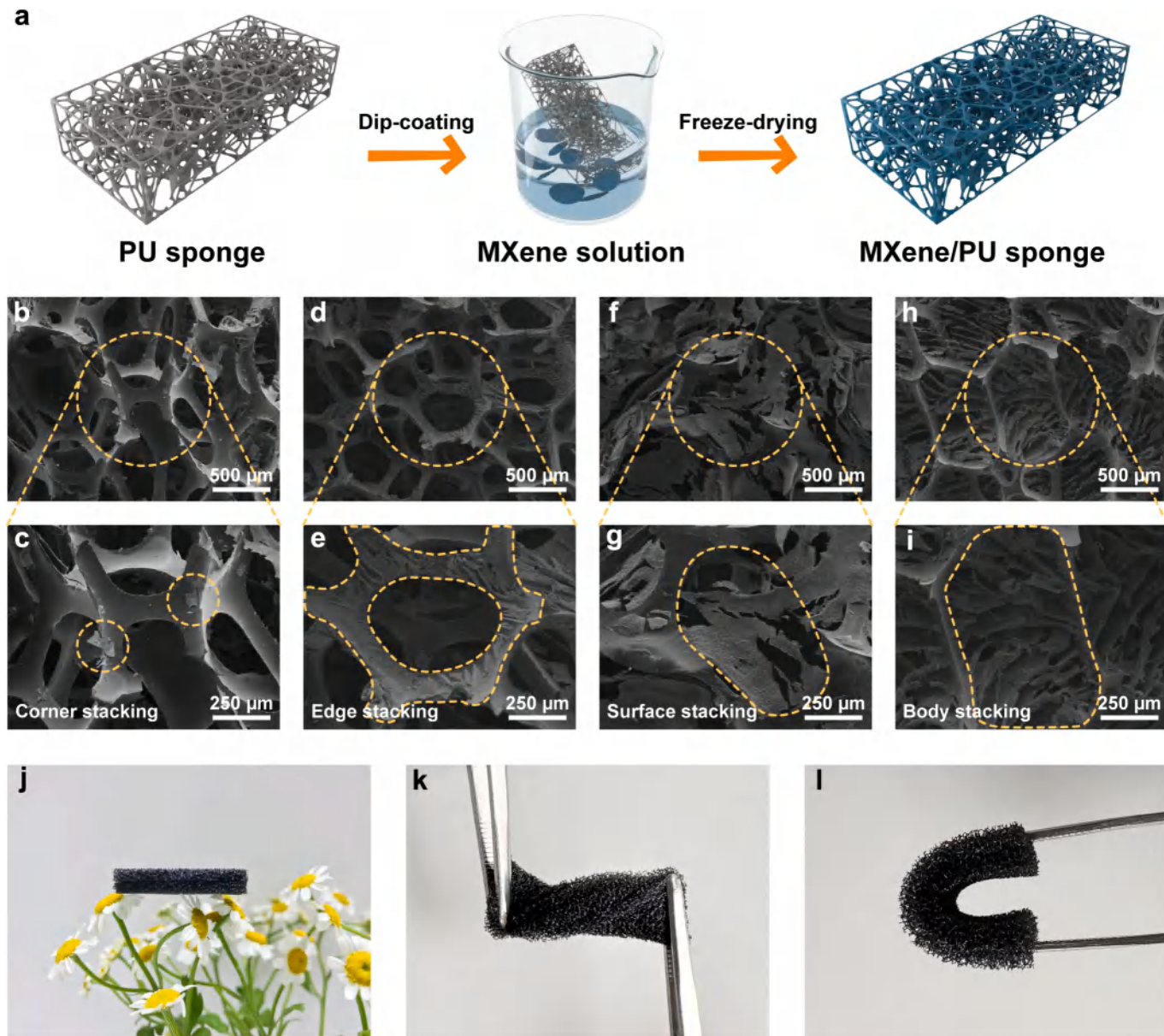


Fig. 2. Design and characterization of MPS and GMPS. a) Schematic illustration of the fabrication procedure of MPS. b-i) The SEM images corresponding to MPS-X ($X = 5, 10, 15$, and 20 mg mL^{-1}). j) The GMPS sample was placed on the top of the flowers. Digital images of GMPS with k) twisting and l) bending.

3D network structure was chosen as the original skeleton [40]. The pristine PU sponge revealed the smooth pore cell surface and micron-sized pores (Fig. S4), which maintained the low density ($\sim 9 \text{ mg cm}^{-3}$) and interconnected porous bracket. Subsequently, the clean PU sponge was soaked in the MXene solution to absorb the $\text{Ti}_3\text{C}_2\text{Tx}$ nanosheet through multiple extrusions. After full immersion, the sponge was frozen quickly and transferred to a freeze dryer for lyophilizing (the details were shown in the experimental section). Finally, it formed the 3D cellular-like network structure where the $\text{Ti}_3\text{C}_2\text{Tx}$ flakes were coated on the skeleton of the sponge (Fig. 2b-i). The filling amount of $\text{Ti}_3\text{C}_2\text{Tx}$ sheets in the MPS composite could be simply adjusted by controlling the concentration of $\text{Ti}_3\text{C}_2\text{Tx}$ MXene solution. For simplicity, “MPS-X” is used to represent the different non-gradient samples, and “X” indicates diverse concentrations of MXene solutions ($X = 5, 10, 15$, and 20 mg mL^{-1}). Fig. S5 shows the diverse MPS modules after the dip-coating of MXene solution and freeze-drying process. The FT-IR spectra of $\text{Ti}_3\text{C}_2\text{Tx}$ MXene and pristine PU sponge show the broad band of $\text{Ti}_3\text{C}_2\text{Tx}$ MXene at 3421 cm^{-1} corresponded to the stretching vibration of the hydroxy

($-\text{OH}$) group, and the peaks of pristine PU sponge at 3373 cm^{-1} and 1537 cm^{-1} were caused by vibration of N-H group (Fig. S6). The disappearing $-\text{OH}$ peak of $\text{Ti}_3\text{C}_2\text{Tx}$ MXene and the weakening N-H peaks of pristine PU sponge in the FT-IR spectra of MPS confirm the existence of hydrogen bonding between $\text{Ti}_3\text{C}_2\text{Tx}$ MXene and PU sponge. From the SEM images (Fig. 2b-g), there existed four representative stacking conditions of $\text{Ti}_3\text{C}_2\text{Tx}$ nanosheets in the pores of PU sponge, namely, corner stacking, edge stacking, surface stacking, and body stacking, as the concentrations of MXene solutions increased from 5 to 20 mg mL^{-1} [35]. Interestingly, a distinctive body stacking structure inside the pore could be observed which was different from the stacking formation previously reported when the concentration increased to 20 mg mL^{-1} (Fig. 2h,i) [35,40,41]. The body stacking means the sponge pores were filled with the few-layer grid structure, which was prepared due to a special freeze-drying process [42]. Every layer of grid structure consisted of a few $\text{Ti}_3\text{C}_2\text{Tx}$ nanosheets, at the same time, there existed gaps with different level widths between adjacent grids, and these grid and gap constructions constituted micro-sponge structures together. The

above four types of MXene sheets in the MPS contributed to the promotion of EMWs absorption and enhancement of thermal-physical properties, which will be discussed later. Fig. 2j shows the light weight of the GMPS that could be placed on the petals of the flowers steadily without deforming them. Concurrently, the GMPS could restore its original shape with obvious twisting, bending, and compression, which displayed excellent mechanical stability (Fig. 2k-l and Fig. S7). Furthermore, the compressive stress-strain curves of MPS and GMPS with different contents of MXene are shown in Fig. S8. Fig. S9 shows the MXene loading in MPS modules under various preparation conditions. Under the same compressive strain, the compressive stress of the MPS increased with the increase in MXene content, especially when the compressive strain exceeded 40%. When the compressive strain was 80%, the compressive strength of the pristine PU sponge was only 42.8 kPa. When 6.9 wt.% MXene was added, the compressive strength of MPS-5 increased to 48.6 kPa. With the further increase of MXene to 34.2 wt.%, the compressive strength of MPS-20 could reach 82.4 kPa. Especially, due to the presence of MPS-20, the compressive stress of different GMPS exhibited a similar trend with a further increase in strain. In addition, as shown in Table S1, the compression performance of GMPS in this study is better than that of similar composite foams reported previously.

3.2. EMI shielding performance of MPS

For the non-gradient conductive MPS modules, two factors were considered in our research, including the intrinsic properties of Ti_3C_2Tx and the microstructure of composites, which were dominated by the adjustment of MXene solution concentration. The intrinsic properties of Ti_3C_2Tx , which include its conductivity and mass loading, denote the essential physical characteristics of the materials. Meanwhile, the microstructure of composites encompasses the distinctive structural features of the 2D nanosheets intrinsic to Ti_3C_2Tx , as well as the array of specific structural characteristics that emerge from the integration with the 3D scaffold of the PU sponge. Collectively, the intrinsic properties of Ti_3C_2Tx and the microstructure of the composites are synergistic, playing pivotal roles in influencing the EMI shielding performance. The average SE_T values in the X-band frequency range of MPS modules with various concentrations of MXene solutions are displayed in Fig. 3a. The EMI SE value defines the ability of samples to block incident radiation, and typically, commercial applications call for samples with an EMI SE value of 20 dB, or 99% attenuation of the waves [35,43]. The EMI SE of MPS composites was almost independent in the X-band, which is consistent with the reported composite foam [40,41,43]. Significantly, the SE_T value of MPS resulted in a substantial elevation from an initial value of approximately 14.3 dB to an impressive maximum of 40.3 dB, effectively attenuating 99.99% of incident EMWs, as the concentration of MXene solution increased to 20 mg mL⁻¹ [35]. Fig. 3b shows the

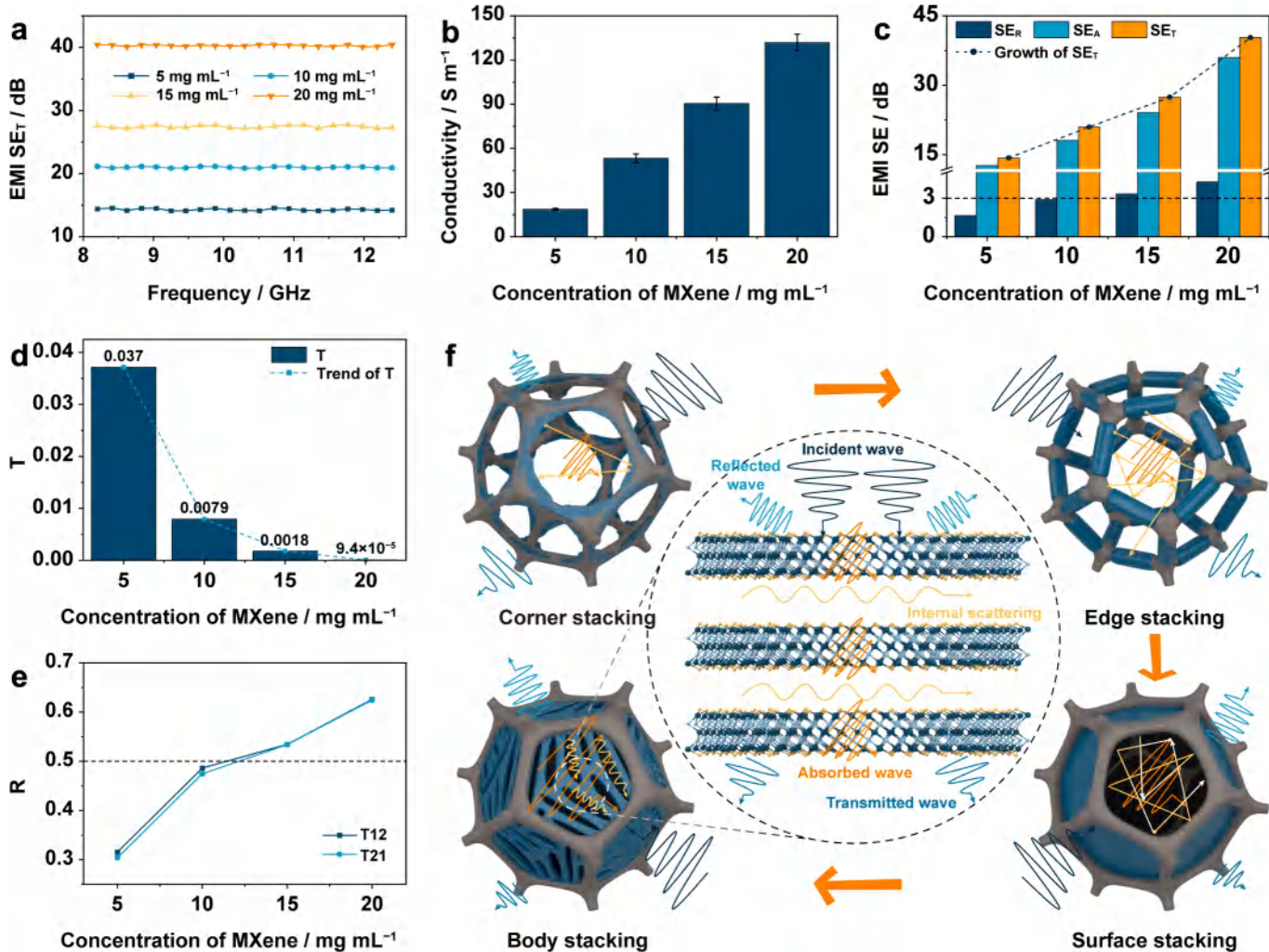


Fig. 3. EMI shielding performance of MPS. a) EMI SE_T , b) conductivity, c) EMI SE (SE_T , SE_A , SE_R), d) T value, and e) R value of MPS with different MXene solution concentrations. f) EMI shielding mechanism for different MPS: corner stacking, edge stacking, surface stacking, and body stacking.

conductivity of MPS modules under diverse preparation conditions. Firstly, the conductivity was depth-dependence on the filling amount of $\text{Ti}_3\text{C}_2\text{Tx}$. Secondly, the variation in MXene loading within MPS modules, corresponding to the increase in MXene solution concentrations, was discernible through the microstructural observations presented in the SEM images (Fig. 2b–i). In particular, the SE_T value of MPS-5 was found to be the least pronounced, a phenomenon principally ascribed to its minimal conductivity and the largest interval between the $\text{Ti}_3\text{C}_2\text{Tx}$ fillers. Achieving elevated values of EMI SE typically necessitates materials that exhibit both high conductivity and a reasonable structural configuration. As depicted in Fig. 2b–i and Fig. 3b,c, with increasing concentrations of MXene solutions, there is a concomitant increase in the conductivity of the MPS, while the structure of $\text{Ti}_3\text{C}_2\text{Tx}$ filler becomes more compact, ultimately leading to an enhancement in the SE_T value of the MPS [35,44].

Furthermore, the EMI SE of MPS could be understood from several hypothesized mechanisms depicted in Fig. 3f. Based on the above analysis, the excellent EMI SE shielding performance of the MPS was attributed to the synergistic effect among the intrinsic properties of $\text{Ti}_3\text{C}_2\text{Tx}$ and the microstructure of the composites. On the one hand, the EMI shielding performance originated from the excellent conductivity and the layered architecture of MXene, mainly including EMWs reflection due to impedance mismatch, multiple loss mechanisms from the interaction between EMWs and MXene, and internal scattering of layer-by-layer $\text{Ti}_3\text{C}_2\text{Tx}$ nanosheets [12,17]. On the other hand, there existed various mechanisms in four typical stacking states of MXene as we mentioned previously, corner stacking, edge stacking, surface stacking, and body stacking, and the four stacking states prolonged the transmission paths of the EMWs in varying degrees through internal multiple scattering (Fig. 2b–i and Fig. 3f) [12,17]. The SE_T value of MPS-5 was just about 14.3 dB with inferior MXene loading (6.9 wt.%) and conductivity (18.70 S m^{-1}) (Fig. 3a–c). The $\text{Ti}_3\text{C}_2\text{Tx}$ flakes were stacking on the corners, which formed a simply conductive network without effective internal scattering, along with a high transmission coefficient ($T = 0.037$) of EMWs (Fig. 2b,c and Fig. 3d,f). Unlike MPS-5, the form of $\text{Ti}_3\text{C}_2\text{Tx}$ flakes to MPS-10 has changed from stacking on the corners to stacking on the edges, which further completed the conductive network with more effective internal scattering (Fig. 2d,e and Fig. 3f). In the process, the SE_T value of MPS-5 increased to 21.0 dB and the T value reduced to 0.0079 (Fig. 3b,d). After the concentration of MXene solution increases to 15 mg mL^{-1} , the nanosheets tend to form the surface stacking structure above the pore (Fig. 2f,g and Fig. 3f). On one side, the separation structures are beneficial to the internal multiple scattering of EMWs, the corresponding SE_T value increased to 27.4 dB. On the other side, it constructed a more intense conductivity pathway which led the conductivity of MPS-15 to increase to 90.47 S m^{-1} , meanwhile, the impedance mismatch was aggravated and R increased to 0.53 (Fig. 3a–c, e). Fig. 2h–i and Fig. 3f displayed that the MXene filler converted to the body stacking structure inside the pore when the MXene solution concentration increased to 20 mg mL^{-1} . At the same time, the internal multiple scattering mechanism turned to take place in the abundant grid regions with microporous structures. The conductivity of MPS-20 increased to 131.95 S m^{-1} , simultaneously, and the R increased to 0.62 due to a larger impedance mismatch for MPS-20 even though the absorption shielding effectiveness (SE_A) value ($\text{SE}_A = 36.0 \text{ dB}$) was much larger than the SE_R value ($\text{SE}_R = 4.2 \text{ dB}$) (Fig. 3a–c,e). This was due to that the EMI SE absorption was the ability of the shield to attenuate EMWs that only penetrate into the material because reflection occurs before absorption [17,45–47]. The shielding mechanism should depend on the value of power coefficients. Therefore, absorption was the main form of shielding for the samples MPS-5 and MPS-10, meanwhile, reflection was the main form of shielding for the samples MPS-15 and MPS-20 based on the power coefficients of T , R , and the absorption coefficient (A) (Fig. S10).

3.3. EMI shielding performance of GMPS

To explore the advantages of gradient-conductive structure in EMI shielding, different gradient types of conductive GMPS were constructed for comparison (Fig. 4). For the non-gradient conductive MPS structure, the incident EMWs are easily reflected at the air-sponge interface owing to high impedance mismatch, which inevitably brings the high secondary radiation pollution of EMWs. In contrast, the gradient-conductive GMPS structure provides an impedance-matching layer, so the incident wave can pass smoothly through the air-sponge interface. And multi-interface reflections are generated among different conductive layers to continuously attenuate EMWs, which can reduce secondary radiation pollution of EMWs. To construct the gradient-conductive structure, two MPS modules with the same or different concentrations of $\text{Ti}_3\text{C}_2\text{Tx}$ MXene solutions were stacked together, “GMPS-X/Y” (X, Y = 5, 10, 15, and 20 mg mL^{-1}) was used to represent the different non-gradient samples, which the “X” and the “Y” indicated the MXene solution concentration of the impedance match layer and the impedance mismatch layer individually. As shown in Fig. 3a–c, test “T12” and test “T21” represent the EMWs incident from the low conductive layer (GMPS-X) and high conductive layer (GMPS-Y), respectively. The SE_T , SE_R , and SE_A values of GMPS with different EMWs incidence directions are shown in Fig. 4a,b. A comparison of different impedance match layers in T12 revealed that the SE_T value increased from 44.6 dB in GMPS-5/20 to 56.2 dB in GMPS-20/20 with increasing MXene concentrations of the resistance match layer in GMPS. Generally speaking, the environmental-friendly EMI shielding materials with low EM reflection mean that the shielding materials show low EM reflection of $R < 0.5$ or $\text{SE}_R < 3 \text{ dB}$ under EMI shielding performance of $\text{SE}_T > 20 \text{ dB}$ [16,17]. As for both GMPS-5/20 and GMPS-10/20, the SE_R values were 0.88 dB and 2.9 dB while the R values were 0.18 and 0.49 (Fig. 4c), suggesting that the EMWs dissipate mainly through absorption. However, the SE_R and R values exceed the critical values of low EM reflection for GMPS-15/20 ($\text{SE}_R = 3.3 \text{ dB}$, $R = 0.53$) and GMPS-20/20 ($\text{SE}_R = 4.1 \text{ dB}$, $R = 0.61$), indicating that as the concentration of MXene within the impedance-matching layer increased, the initial sponge changed from impedance-matching to impedance-mismatching. Consequently, incident electromagnetic waves are almost entirely reflected into free space, leading to secondary EM pollution. At the same time, the trends of EMI SE and R in GMPS were similar to those in single-layer MPS. For GMPS in T21, the SE_T values were essentially consistent with the values in T12, while the SE_R and R values were largely unchanged (closer to the MPS-20). Therefore, taking into account both R and SE_T , GMPS-5/20 stood out as the premier choice for eco-friendly EMI shielding materials.

The influence of the gradient-conductive structure of GMPS-5/20 on the EMI shielding performance of the composite was further verified by finite element analyses. Based on SEM images of the sponge (Fig. S4), a sponge model with an aperture of 1.1 mm and dimensions of $22.86 \text{ mm} \times 10.16 \text{ mm} \times 3 \text{ mm}$ was established (Fig. S11). According to microwave theory, the TE_{10} mode is the dominant mode that propagates inside the WR-90 waveguide operating in the X-band [48]. Finite element simulation software has been used for the waveguide simulation and representation of the EMWs along the waveguide. Boundary conditions inside a WR-90 waveguide are described in reference [48]. Fig. 4d,e and Fig. S12,S13 show the section plot of electric field norm, arrow plot (orange arrows) of power flow, and isosurface plot of electric field norm of MPS-5, MPS-20, and GMPS-5/20 tested with different EMWs incident directions. Calculations of theoretical simulations of EMI SE, R , and A values for various modules were performed, closely aligning with the outcomes obtained from experiments (Fig. 4f–i and Fig. S12,S13). The partial consistency between the theoretical simulation and the experimental results could be due to the existence of insignificant gaps at the interlayer interface of the modules and the measurement inaccuracies [31]. When the EMWs passed through the GMPS-5/20 from port 1 to port 2 (or from port 2 to port 1), the electric field was highly attenuated. The situation was similar in the MPS-20. However, for the MPS-5, the

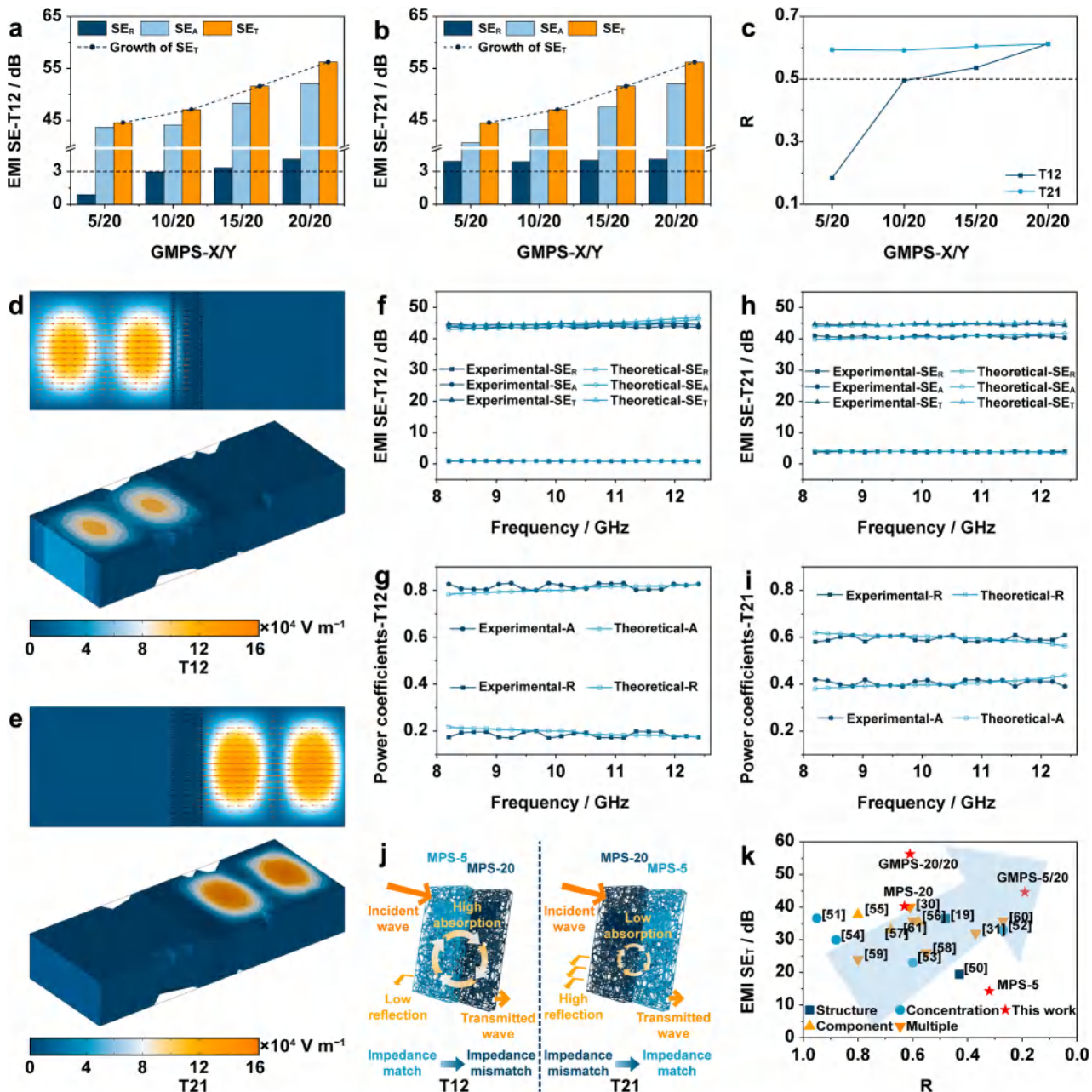


Fig. 4. EMI shielding performance of GMPS. The EMI SE (SE_T , SE_A , SE_R) of GMPS in a) T12 and b) T21. c) The R value of GMPS in T12 and T21. The section plot of electric field norm, arrow plot (orange arrows) of power flow, and isosurface plot of electric field norm of GMPS-5/20 in d) T12 and e) T21 at 12.4 GHz. FEA results and experimental results of f) EMI SE and g) R, A, T values of GMPS-5/20 in T12 in the X-band. FEA results and experimental results of h) EMI SE and i) R, A, T values of GMPS-5/20 in T21 in the X-band. j) The schematic illustration of the EMI shielding mechanism of GMPS-5/20 in T12 and T21. k) Comparison of EMI SE_T and R of MPS and GMPS with other EMI shielding materials of different gradient types.

attenuation of EMWs was less obvious, and the arrows representing the power flow could still be observed on the right side of the MPS-5. Fig. 4d, e show that the power flow arrows passed through MPS-5 and ended at the junction of MPS-5 and MPS-20 when the EMWs were incident from port 1, but the arrows were hardly entered into MPS-20 when the EMWs were incident from port 2. This also corresponds to the different R and SE_R values acquired when the EMWs were incident from different directions of GMPS-5/20 in the previous occurrence, and explains the reason that GMPS-5/20 with a distinct gradient structure could produce a shielding effect dominated by the absorption of EMWs. In the same way, the isosurface of the electric field norm of MPS-5, MPS-20, and GMPS-5/20 was also an analogous statement.

The schematic diagram of the EMI shielding mechanism of GMPS-5/

20 is shown in Fig. 4j. In general, the ultrahigh EMI shielding performance of MPS and GMPS is attributed to the synergistic interplay between the intrinsic properties of Ti_3C_2Tx MXene and the microstructure of the composites, as well as the ingenious design of the customizable gradient structure. These factors lead to multiple shielding mechanisms, including reflection and absorption at abundant interfaces. Especially, high-concentration MXene provides an efficient conductive network that enables reflection shielding at the interface. When the EMWs are incident from the high-conductive layer (MPS-20) of GMPS-5/20, the vast majority of the EMWs are immediately reflected into free space due to the impedance mismatching of air-sponge interfaces, causing secondary contamination of EMWs. However, when the EMWs are incident from the low-conductive layer (MPS-5) of GMPS-5/20, a small portion of

the EMWs is reflected into the air due to the impedance matching of the air-sponge interfaces. Meanwhile, the residual EMWs entering the composites generate internal multiple reflections among the porous structures of the sponge and the multi-level structure of MXene, dissipating EMWs through conductive loss, which effectively improves the absorption ability of GMPS-5/20 to EMWs. In particular, due to the great difference in electrical conduction between MPS-5 and MPS-20, the polarization phenomenon at their interface further enhances the attenuation of EMWs. Therefore, incident EMWs from the low-conductive

layer were favorable for the high absorption of the EMWs, which highlights the advantages of the unique asymmetric conductive structure. The EMI shielding performance of MPS, GMPS, and other composites reported in the literature was compared and analyzed (Table S2). Fig. 4k shows the comparison of EMI SE versus R for EMI shielding materials with different gradient types. The GMPS-5/20 prepared in this work achieves high EMI SE (44.6 dB) with a small R of 0.18, which is superior to similar materials reported [19,30,31,49–60].

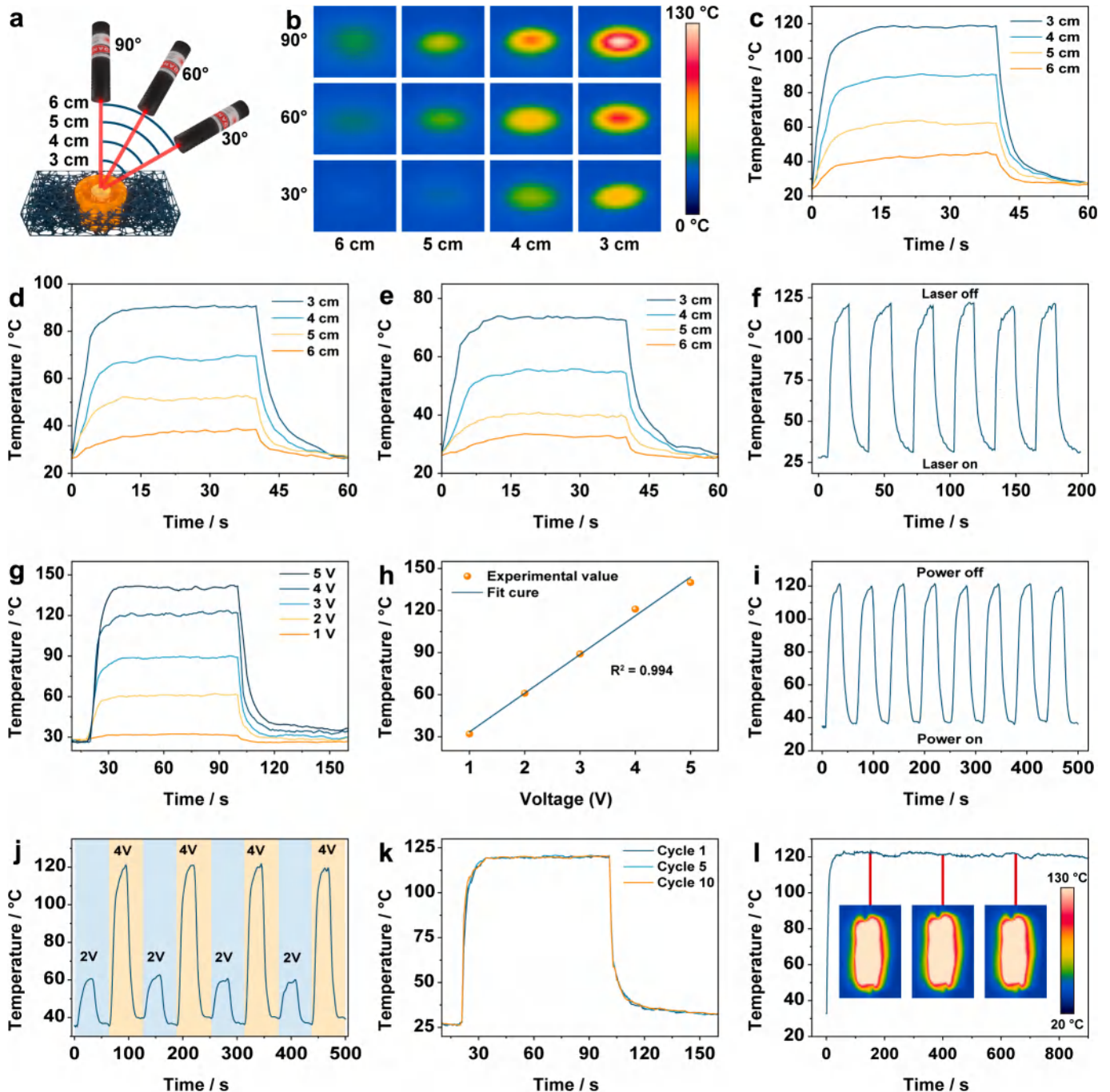


Fig. 5. Photothermal and electrothermal conversion performance of GMPS. a) Schematic diagram of the GMPS irradiated with an NIR laser lamp (808 nm, 100 mW cm⁻²). b) IR images of the GMPS at central maximum temperature irradiated from different angles and distances. Temperature evolution with increasing time at different radiation distances and incident angles: c) 90°, d) 60°, and e) 30°. f) Thermal response of GMPS under an NIR laser lamp for six on/off cycles. g) Electrothermal conversion performance of GMPS at different driving voltages. h) Experimental data and linear fitting of saturation temperature versus voltages. i) The thermal response of GMPS for eight on/off cycles at 4 V. j) Thermal response of GMPS switching at 2 and 4 V. k) Joule heating cycles of GMPS at 4 V. l) Temperature evolution curve of GMPS at 4 V and inserted IR images.

3.4. Photothermal and electrothermal conversion performance of GMPS

The UV-vis-NIR absorption spectra of the $\text{Ti}_3\text{C}_2\text{Tx}$ nanosheets reveal a distinctive absorption in the NIR region, ranging from 750 to 850 nm, which is comparable to conventional metal nanoparticles exhibiting the LSPR effect (Fig. S14) [61]. According to previous research, the body stacking structure inside the pores of MPS-20 endowed GMPS-20/20 with excellent EMI shielding ability, which was an essential prerequisite for the photothermal conversion property. The internal scattering in the grids inside the pores of composites and the LSPR effect of $\text{Ti}_3\text{C}_2\text{Tx}$ filler provide efficient light absorption [62]. Fig. 5a-f displays the photothermal performance of a GMPS-20/20 heater (22.86 mm × 10.16 mm × 6 mm) exposed to a NIR laser source (808 nm, 100 mW cm⁻²). To explore the photothermal conversion capacity of GMPS-20/20, we measured and recorded different temperature evolutions with an infrared (IR) thermal imaging camera by changing the incident angles (90°, 60°, and 30°) and radiation distances (6, 5, 4, and 3 cm) of the laser source (Fig. 5a). The IR images vividly show the saturated temperature (central maximum) under different irradiation conditions. It was seen that the saturated temperature reached the maximum value (119 °C) when the laser was vertical to (90°) the heater at the radiation distance of 3 cm (Fig. 5b). Fig. 5c-e shows that the temperature of the GMPS-20/20 heater exhibited a linear increase, reached saturation temperature around 10 s, and maintained stability until the light was turned off at 40 s. Then, the temperature dropped rapidly from the saturation value to room temperature. A series of temperature variations indicate that the GMPS-20/20 has outstanding photothermal conversion performance with high sensitivity and stability [63]. And the photothermal performance of the GMPS-20/20 heater could be regulated by changing the incident angle and distance of the illuminant. Furthermore, the photothermal cycle stability of the GMPS-20/20 was demonstrated through repeated laser on/off tests for six times within 200 s, and each cycle included consecutive photothermal heating (15 s) and cooling (15 s) (Fig. 5f). Compared to various previously reported photothermal converters based on 3D porous foam structures, the GMPS-20/20 exhibits superior photothermal conversion capability (Table S3). To conclude, the superb photothermal conversion performance endows the GMPS-20/20 heater with a quick response (10 s), high stability, a wide temperature window (from 32 to 119 °C), and high light sensitivity, which were suitable for practical applications including photothermal therapy, solar photothermal electrode, and wearable device, etc.

It should be noted that the excellent heating performance of a photothermal heater is meaningless at night and on cloudy or rainy days, which greatly limits the popularity of the heater. It is imperative to develop dual-energy driving heaters beyond luminous energy. The potential electrothermal conversion performance of GMPS, based on the high conductivity (131.95 S m⁻¹) of MPS-20, provides an effective solution to the above problem. Fig. S15, shows that the GMPS-20/20 could illuminate a red LED bulb when connected as a wire to an electrochemical workstation (CHI 660E, 1.5 V). This is expected to exhibit electrothermal conversion performance based on the relationship between current and resistance [63]. Fig. 5g-l displays the Joule heating capability of the GMPS-20/20 (22.86 mm × 10.16 mm × 6 mm) by applying various steady input voltages (from 1 to 5 V) and recording the temperature evolution with the IR camera. Under an applied voltage of 5 V, the surface temperature of the GMPS-20/20 increased rapidly, reaching a saturated temperature of 140 °C within only 15 s, and decreased to a steady-state temperature in approximately 30 s after the power was cut off (Fig. 5g). This reflects the rapid thermal response of GMPS. In the case of driving voltages of remaining values, the temperature evolution exhibits a similar trend to that of the 5 V. Meanwhile, the saturated temperature decreases with reducing driving voltages. Impressively, a high saturation temperature of approximately 60 °C was achieved within 15 s with a low operating voltage of 2 V, demonstrating excellent Joule heating capability. At the same time, the extremely low driving voltage not only ensures safety during application but also

reduces energy consumption. The linear fitting of saturated temperatures versus driving voltages confirms that the GMPS-20/20 has low but steady resistance and high heating controllability, which could be achieved by adjusting the driving voltage (Fig. 5h). Furthermore, the temperature variation curve of GMPS-20/20 remains consistent when a voltage of 4 V is repeatedly applied and removed (Fig. 5i). The maximum value of the surface temperature of GMPS-20/20 remains basically unchanged when the voltage is repeatedly switched between 2 and 4 V (Fig. 5j). These further prove the stability and temperature adjustability of GMPS-20/20 heaters. To evaluate the cyclic stability of the GMPS-20/20 heater, the surface temperature curves were measured following the previous method for the 1st, 5th, and 10th cycles at 4 V (Fig. 5k). The overlapping temperature curves indicate that the heater has stable cyclic heating performance. Fig. 5l shows that the GMPS-20/20 heater could maintain a uniform temperature distribution and sustain a saturated temperature at an input voltage of 4 V for over 800 s. Compared to other similar electrothermal conversion systems based on 3D porous foam structures reported, the GMPS-20/20 fabricated in this study exhibited a higher surface temperature (140 °C) at a lower driving voltage (5 V) (Table S4). Overall, the above analysis reveals that the GMPS-20/20 heater, based on electrothermal conversion, has wide temperature adjustability (from 31 to 140 °C), low driving voltage (from 1 to 5 V), fast thermal response (15 s), and superior Joule heating reliability (over 800 s). The excellent electrothermal conversion performance meant that the GMPS heaters could be used in thermotherapy, keeping warm, melting ice, or industrial applications where heating is needed.

3.5. EMI shielding, photothermal, and electrothermal conversion applications of GMPS

To demonstrate the modular properties for multi-application scenarios of GMPS and evaluate the EMI shielding, photothermal, and electrothermal conversion performance, practical application simulations were performed in Fig. 6. To further simulate real-world scenarios, the large-size MPS-5 and MPS-20 samples were prepared (both sizes were 200 mm × 200 mm × 3 mm) (Fig. S16). Then the MPS samples were cut into different sizes according to the size of the wooden house model. Among them, the GMPS-5/20 and GMPS-20/20 were used as EMI shielding wallpaper to be pasted on the inner wall and the outdoor roof, respectively. Meanwhile, the GMPS-20/20 was used as a photothermal and electrothermal heating device (Fig. 6a). A wireless power transfer system utilizing a BD243 Tesla coil, operating at a frequency of 6.356 MHz, was used as the EMWs emission source [13]. The working principle of the Tesla coil is depicted in Fig. S17. When the Tesla coil was activated, the energy-saving lamps (5 W) placed both indoors and outdoors could be lit, and the EMR inside the house reached values of 1261 V m⁻¹ and 122 µT (Fig. S18). The safety levels for electric and magnetic field radiation are 12 V m⁻¹ and 10 µT, respectively [13]. However, when the GMPS-5/20 was pasted on indoor walls between the Tesla coil and the energy-saving lamp, the lamp placed outdoors was still lit while the lamp placed indoors went out instantly and the electric and magnetic field values around the house reached safe levels of 0 V m⁻¹ and 1.85 µT (Fig. 6b). This phenomenon indicates that the GMPS-5/20 sample effectively blocked the EMWs signals and successfully realized the EMI shielding. Similarly, when the GMPS-20/20 with higher SE_T was pasted on the outdoor roof, the lamp placed indoors went out, and the EMR values inside the house reduced from 1166 V m⁻¹ and 118 µT to 0 V m⁻¹ and 0 µT at the same time (Fig. S19,S20). Furthermore, the GMPS-5/20 pasted on indoor walls could absorb more EMWs than GMPS-20/20 due to its lower R based on previous research, so the modular design of GMPS provides multiple choices based on different application scenarios and provides multiple guarantees for the health of people.

In addition, we studied the photothermal conversion performance of the GMPS-20/20 heater exposed to sunlight at 10:00 am and 12:00 noon and recorded the surface temperature with an IR camera (Fig. 6c). The

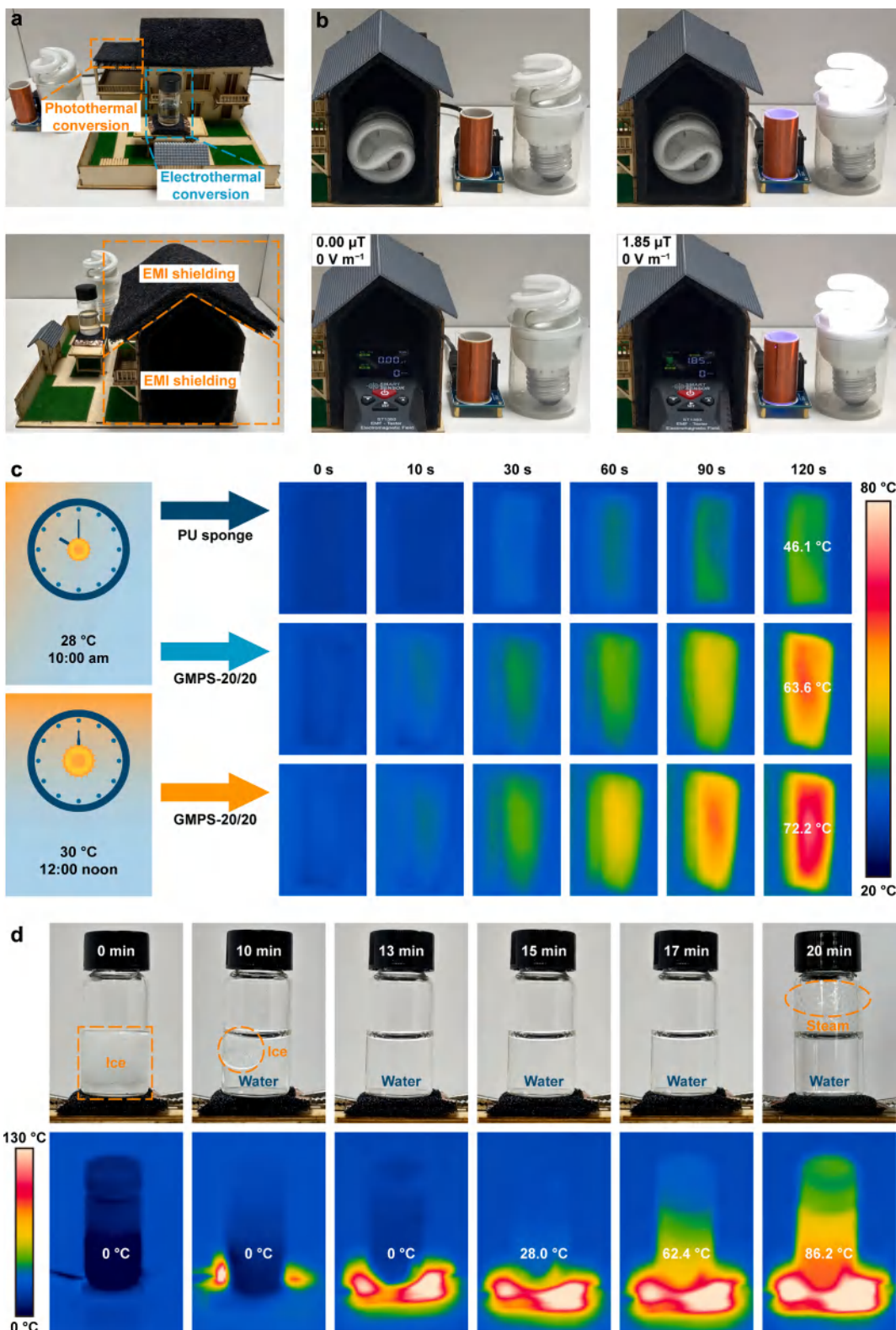


Fig. 6. EMI shielding, photothermal and electrothermal conversion application of GMPS. a) The digital images of EMI shielding, photothermal, and electrothermal conversion application simulations design. b) The digital images depicting changes in the energy-saving lamps (5 W) and EMR values with the GMPS-5/20 pasted indoors under the influence of the turn-off or turn-on Tesla coil. c) The digital images of the sun and the infrared images of pristine PU sponge and GMPS-20/20 exposed to sunlight at 10:00 am and 12:00 noon (Nanjing, China, Sept. 18, 2023). d) The digital images of the bottom ice/water with increasing time during the deicing process on the GMPS-20/20 at a driving voltage of 4 V.

surface central maximum temperature of the GMPS heater rapidly increased from the ambient temperature of 28.0 °C to the saturated temperature of 63.6 °C within 120 s at 10:00 am, nevertheless, the pristine PU sponge only increased to 46.1 °C with the same condition. At 12:00 noon, in comparison, the surface temperature of the GMPS-20/20 heater exhibited more remarkable temperature change during the sunlight irradiation, and the saturated temperature reached 72.2 °C within 120 s. The above results show that the Ti_3C_2Tx nanosheets filler and special construction of composite sponge warranted an efficient light absorption over the near-infrared spectrum and full-spectrum solar light. Then, we assembled electrothermal deicing equipment based on the Joule heating capability of the GMPS heater, which was connected to a driven voltage of 4 V through copper foils and crocodile clips. From Fig. 6d, the ice (5 g) in a glass bottle was completely converted to water within around 13 min. As the heating continued, the water temperature increased to nearly 86.2 °C with steam visible after a further 7 min. By contrast, the identical ice melted completely within 55 min at normal temperature (Fig. S21). In conclusion, the GMPS-20/20 has outstanding electrothermal and photothermal dual-driven characteristics and realizes all-weather and continuous heating, which can be suitable for applications in multiple scenes.

4. Conclusion

In summary, the customizable GMPS modules with hierarchical porous structure gradient and MXene concentration gradient were presented in this work. The GMPS modules, featuring an asymmetric gradient structure, were constituted of various MPS modular units that underwent the dip-coating and freeze-drying processes. Based on the synergistic interactions of the hierarchical porous skeleton and MXene constituent, the GMPS-5/20 exhibited an exceptional average EMI SE (44.6 dB) and low reflection ($R = 0.18$). Within this absorption-dominated architecture, the low-conductivity layers of corner stacking (MPS-5) acted as EM absorption layers, while the high-conductivity layers of body stacking (MPS-20) served as EM reflection layers. The FEA simulations and numerical models, which illustrated the influence of asymmetric gradient structures on the EMI shielding performance and the ultra-low R value for GMPS modules, were consistent with the experimentally measured results. Furthermore, the GMPS modules exhibited excellent thermal management capability, which was more attractive in EMI shielding materials. The exceptional comprehensive performance enables the GMPS modules with promising application prospects in intelligent residences, multifunctional integrated systems, and other fields.

CRediT authorship contribution statement

Yuhui Feng: Writing – original draft, Software, Investigation. **Min-gye Zhu:** Data curation. **Wenjun He:** Validation, Methodology. **Yan Bai:** Formal analysis. **Ning Ding:** Methodology. **Zhen You:** Software. **Xiang Zou:** Validation. **Weiwei Zhao:** Methodology. **Shujuan Liu:** Writing – review & editing, Funding acquisition, Conceptualization. **Qiang Zhao:** Writing – review & editing, Funding acquisition, Conceptualization.

Declaration of competing interest

The authors declare that they have no known competing financial interests or personal relationships that could have appeared to influence the work reported in this paper.

Data availability

No data was used for the research described in the article.

Acknowledgements

The authors gratefully acknowledge the project supported by the National Natural Science Foundation of China (62288102, 62375142).

Appendix A. Supplementary data

Supplementary data to this article can be found online at <https://doi.org/10.1016/j.cej.2024.155959>.

References

- [1] M. Han, D. Zhang, C.E. Shuck, B. McBride, T. Zhang, R. Wang, K. Shevchuk, Y. Gogotsi, Electrochemically modulated interaction of MXenes with microwaves, *Nat. Nanotechnol.* 18 (2023) 373–379, <https://doi.org/10.1038/s41565-022-01308-9>.
- [2] A. Iqbal, F. Shahzad, K. Hantanasisirakul, M.K. Kim, J. Kwon, J. Hong, H. Kim, D. Kim, Y. Gogotsi, C.M. Koo, Anomalous absorption of electromagnetic waves by 2D transition metal carbonitride Ti_3CNT_x (MXene), *Science* 369 (2020) 446–450, <https://doi.org/10.1126/science.aba7977>.
- [3] M. Dadashi Firouzjaei, S.K. Nemanic, M. Sadrzadeh, E.K. Wujcik, M. Elliott, B. Anasori, Life-cycle assessment of Ti_3C_2Tx MXene synthesis, *Adv. Mater.* 35 (2023) 2300422, <https://doi.org/10.1002/adma.202300422>.
- [4] T. Zhou, Y. Yu, B. He, Z. Wang, T. Xiong, Z. Wang, Y. Liu, J. Xin, M. Qi, H. Zhang, X. Zhou, L. Gao, Q. Cheng, L. Wei, Ultra-compact MXene fibers by continuous and controllable synergy of interfacial interactions and thermal drawing-induced stresses, *Nat. Commun.* 13 (2022) 4564, <https://doi.org/10.1038/s41467-022-32361-6>.
- [5] N. Wu, Y. Yang, C. Wang, Q. Wu, F. Pan, R. Zhang, J. Liu, Z. Zeng, Ultrathin cellulose nanofiber assisted ambient-pressure-dried, ultralight, mechanically robust, multifunctional MXene aerogels, *Adv. Mater.* 35 (2023), <https://doi.org/10.1002/adma.202207969>.
- [6] Y. He, J. Yang, W. Chen, W. Chen, L. Zhao, W. Qi, Gallium-doped MXene/cellulose nanofiber composite membranes with electro/photo thermal conversion property for high performance electromagnetic interference shielding, *Chem. Eng. J.* 464 (2023) 142565, <https://doi.org/10.1016/j.cej.2023.142565>.
- [7] L. Zhuang, D. Lu, J. Zhang, P. Guo, L. Su, Y. Qin, P. Zhang, L. Xu, M. Niu, K. Peng, H. Wang, Highly cross-linked carbon tube aerogels with enhanced elasticity and fatigue resistance, *Nat. Commun.* 14 (2023) 3178, <https://doi.org/10.1038/s41467-023-38664-6>.
- [8] S.A. Hashemi, A. Ghaffarkhah, M. Goodarzi, A. Nazemi, G. Banville, A.S. Milani, M. Soroush, O.J. Rojas, S. Ramakrishna, S. Wuttke, T.P. Russell, M. Kamkar, M. Arjmand, Liquid-templating aerogels, *Adv. Mater.* 35 (2023) 2302826, <https://doi.org/10.1002/adma.202302826>.
- [9] F. Pan, Y. Shi, Y. Yang, H. Guo, L. Li, H. Jiang, X. Wang, Z. Zeng, W. Lu, Poriferan-inspired lightweight, thin, wrinkle-resistance, and multifunctional MXene foam, *Adv. Mater.* (2024) 2311135, <https://doi.org/10.1002/adma.202311135>.
- [10] A. VahidMohammadi, J. Rosen, Y. Gogotsi, The world of two-dimensional carbides and nitrides (MXenes), *Science* 372 (2021) eabf1581, <https://doi.org/10.1126/science.abf1581>.
- [11] C. Tan, Z. Dong, Y. Li, H. Zhao, X. Huang, Z. Zhou, J.W. Jiang, Y.Z. Long, P. Jiang, T.Y. Zhang, B. Sun, A high performance wearable strain sensor with advanced thermal management for motion monitoring, *Nat. Commun.* 11 (2020) 3530, <https://doi.org/10.1038/s41467-020-17301-6>.
- [12] A. Iqbal, P. Sambyal, C.M. Koo, 2D MXenes for electromagnetic shielding: A review, *Adv. Funct. Mater.* 30 (2020) 2000883, <https://doi.org/10.1002/adfm.202000883>.
- [13] X. Ma, S. Liu, H. Luo, H. Guo, S. Jiang, G. Duan, G. Zhang, J. Han, S. He, W. Lu, K. Zhang, MOF@wood derived ultrathin carbon composite film for electromagnetic interference shielding with effective absorption and electrothermal management, *Adv. Funct. Mater.* (2023) 2310126, <https://doi.org/10.1002/adfm.202310126>.
- [14] M. Cheng, M. Ying, R. Zhao, L. Ji, H. Li, X. Liu, J. Zhang, Y. Li, X. Dong, X. Zhang, Transparent and flexible electromagnetic interference shielding materials by constructing sandwich AgNW@MXene/wood composites, *ACS Nano* 16 (2022) 16996–17007, <https://doi.org/10.1021/acsnano.2c07111>.
- [15] T. Xue, Y. Yang, D. Yu, Q. Wali, Z. Wang, X. Cao, W. Fan, T. Liu, 3D printed integrated gradient-conductive MXene/CNT/polyimide aerogel frames for electromagnetic interference shielding with ultra-low reflection, *Nano-Micro Lett.* 15 (2023) 45, <https://doi.org/10.1007/s40820-023-01017-5>.
- [16] X. Jia, Y. Li, B. Shen, W. Zheng, Evaluation, fabrication and dynamic performance regulation of green EMI-shielding materials with low reflectivity: a review, *Compos. Pt. B-Eng.* 233 (2022) 109652, <https://doi.org/10.1016/j.compositesb.2022.109652>.
- [17] M. Peng, F. Qin, Clarification of basic concepts for electromagnetic interference shielding effectiveness, *J. Appl. Phys.* 130 (2021) 225108, <https://doi.org/10.1063/5.0075019>.
- [18] G. Wang, D. Lai, X. Xu, Y. Wang, Lightweight, stiff and heat-resistant bamboo-derived carbon scaffolds with gradient aligned microchannels for highly efficient EMI shielding, *Chem. Eng. J.* 446 (2022) 136911, <https://doi.org/10.1016/j.cej.2022.136911>.
- [19] R. Haataja, S. Myllymäki, O. Laitinen, H. Jantunen, H. Liimatainen, Controlling the cell and surface architecture of cellulose nanofiber/PVA/ Ti_3C_2Tx MXene hybrid

- cryogels for optimized permittivity and EMI shielding performance, *Mater. Des.* 228 (2023) 111855, <https://doi.org/10.1016/j.matdes.2023.111855>.
- [20] Z. Liu, G. Wang, P. Li, F. Xue, Z. Chen, H. Zheng, R. Ding, J. Xiong, Q. Yan, L. Xu, X. Zhao, Q. Peng, X. He, Gradient in-plane oriented porous carbon inspired by fabrication of toasts for elegant EMI shielding performance, *Carbon* 207 (2023) 136–143, <https://doi.org/10.1016/j.carbon.2023.03.013>.
- [21] T. Kim, H.W. Do, K.J. Choi, S. Kim, M. Lee, T. Kim, B.K. Yu, J. Cheon, B. Min, W. Shim, Layered aluminum for electromagnetic wave absorber with near-zero reflection, *Nano Lett.* 21 (2021) 1132–1140, <https://doi.org/10.1021/acs.nanolett.0c04593>.
- [22] X. Jia, B. Shen, L. Zhang, W. Zheng, Construction of compressible polymer/MXene composite foams for high-performance absorption-dominated electromagnetic shielding with ultra-low reflectivity, *Carbon* 173 (2021) 932–940, <https://doi.org/10.1016/j.carbon.2020.11.036>.
- [23] M. Ma, X. Liang, W. Tao, Q. Peng, W. Shao, S. Chen, Y. Shi, H. He, Y. Zhu, X. Wang, Waterborne polyurethane aerogel with asymmetric gradient structure formed by density-induced self-stratification for absorption-dominated electromagnetic interference shielding, *Compos. Struct.* 342 (2024) 118259, <https://doi.org/10.1016/j.compstruct.2024.118259>.
- [24] M. Ma, X. Liao, Q. Chu, S. Chen, Y. Shi, H. He, X. Wang, Construction of gradient conductivity cellulose nanofiber/MXene composites with efficient electromagnetic interference shielding and excellent mechanical properties, *Compos. Sci. Technol.* 226 (2022) 109540, <https://doi.org/10.1016/j.compscitech.2022.109540>.
- [25] M. Ma, W. Tao, X. Liao, S. Chen, Y. Shi, H. He, X. Wang, Cellulose nanofiber/MXene/FeCo composites with gradient structure for highly absorbed electromagnetic interference shielding, *Chem. Eng. J.* 452 (2023) 139471, <https://doi.org/10.1016/j.cej.2022.139471>.
- [26] J. Yang, X. Liao, G. Wang, J. Chen, F. Guo, W. Tang, W. Wang, Z. Yan, G. Li, Gradient structure design of lightweight and flexible silicone rubber nanocomposite foam for efficient electromagnetic interference shielding, *Chem. Eng. J.* 390 (2020) 124589, <https://doi.org/10.1016/j.cej.2020.124589>.
- [27] K. Sushmita, D. Ghosh, S. Nilawar, S. Bose, Absorption dominated directional electromagnetic interference shielding through asymmetry in a multilayered construct with an exceptionally high green index, *ACS Appl. Mater. Interfaces* 14 (2022) 49140–49157, <https://doi.org/10.1021/acsmami.2c13704>.
- [28] H. Duan, H. Zhu, J. Gao, D.X. Yan, K. Dai, Y. Yang, G. Zhao, Y. Liu, Z.M. Li, Asymmetric conductive polymer composite foam for absorption dominated ultra-efficient electromagnetic interference shielding with extremely low reflection characteristics, *J. Mater. Chem. A* 8 (2020) 9146–9159, <https://doi.org/10.1039/DOTA01393E>.
- [29] Z. Lei, D. Tian, X. Liu, J. Wei, K. Rajavel, T. Zhao, Y. Hu, P. Zhu, R. Sun, C.P. Wong, Electrically conductive gradient structure design of thermoplastic polyurethane composite foams for efficient electromagnetic interference shielding and ultra-low microwave reflectivity, *Chem. Eng. J.* 424 (2021) 130365, <https://doi.org/10.1016/j.cej.2021.130365>.
- [30] J. Yang, Y. Chen, B. Wang, Y. Zhou, X. Chai, X. Yan, W. Han, C. Liu, P. Lin, Y. Xia, H. Zhang, X. Liao, Gradient structure silicone rubber composites for selective electromagnetic interference shielding enhancement and low reflection, *Compos. Sci. Technol.* 229 (2022) 109688, <https://doi.org/10.1016/j.compscitech.2022.109688>.
- [31] M. Li, M. Zhang, Y. Zhao, S. Jiang, Q. Xu, F. Han, J. Zhu, L. Liu, A. Ge, Multilayer structured CNF/rGO aerogels and rGO film composites for efficient electromagnetic interference shielding, *Carbohydr. Polym.* 286 (2022) 119306, <https://doi.org/10.1016/j.carbpol.2022.119306>.
- [32] Z. Du, C. Zhou, H.Y. Mi, H. Li, Z. Qin, R. Xu, Y. Wang, C. Liu, C. Shen, Recorded low-reflection in gradient MXene-decorated melamine microwave shielding foam integrated with piezoresistive sensing and energy absorption properties, *Compos. Pt. A-Appl. Sci. Manuf.* 173 (2023) 107694, <https://doi.org/10.1016/j.jcompositesa.2023.107694>.
- [33] M. Li, H. Liao, J. Wang, Multifunctional composite with porous gradient structure for absorption-oriented ultrahigh electromagnetic interference shielding, *Compos. Pt. A-Appl. Sci. Manuf.* 173 (2023) 107637, <https://doi.org/10.1016/j.jcompositesa.2023.107637>.
- [34] W. Zhao, J. Peng, W. Wang, B. Jin, T. Chen, S. Liu, Q. Zhao, W. Huang, Interlayer hydrogen-bonded metal porphyrin frameworks/MXene hybrid film with high capacitance for flexible all-solid-state supercapacitors, *Small* 15 (2019) 1901351, <https://doi.org/10.1002/smll.201901351>.
- [35] W. Shui, J. Li, H. Wang, Y. Xing, Y. Li, Q. Yang, X. Xiao, Q. Wen, H. Zhang, $Ti_3C_2T_x$ MXene sponge composite as broadband terahertz absorber, *Adv. Opt. Mater.* 8 (2020) 2001120, <https://doi.org/10.1002/adom.202001120>.
- [36] M. Shekhirev, C.E. Shuck, A. Sarycheva, Y. Gogotsi, Characterization of MXenes at every step, from their precursors to single flakes and assembled films, *Prog. Mater. Sci.* 120 (2021) 100757, <https://doi.org/10.1016/j.pmatsci.2020.100757>.
- [37] M. Alhabeb, K. Maleski, B. Anasori, P. Lelyukh, L. Clark, S. Sin, Y. Gogotsi, Guidelines for synthesis and processing of two-dimensional titanium carbide ($Ti_3C_2T_x$ MXene), *Chem. Mat.* 29 (2017) 7633–7644, <https://doi.org/10.1021/acs.chemmater.7b02847>.
- [38] M. Naguib, M. Kurtoglu, V. Presser, J. Lu, J. Niit, M. Heon, L. Hultman, Y. Gogotsi, M.W. Barsoum, Two-dimensional nanocrystals produced by exfoliation of Ti_3AlC_2 , *Adv. Mater.* 23 (2011) 4248–4253, <https://doi.org/10.1002/adma.201102306>.
- [39] O. Mashtalar, M. Naguib, V.N. Mochalin, Y. Dall'Agne, M. Heon, M.W. Barsoum, Y. Gogotsi, Intercalation and delamination of layered carbides and carbonitrides, *Nat. Commun.* 4 (2013) 1716, <https://doi.org/10.1038/ncomms2664>.
- [40] L. Jin, W. Cao, P. Wang, N. Song, P. Ding, Interconnected MXene/graphene network constructed by soft template for multi-performance improvement of polymer composites, *Nano-Micro Lett.* 14 (2022) 133, <https://doi.org/10.1007/s40820-022-00877-7>.
- [41] W. Ma, W. Cai, W. Chen, P. Liu, J. Wang, Z. Liu, A novel structural design of shielding capsule to prepare high-performance and self-healing MXene-based sponge for ultra-efficient electromagnetic interference shielding, *Chem. Eng. J.* 426 (2021) 130729, <https://doi.org/10.1016/j.cej.2021.130729>.
- [42] X. Wang, L. Dong, W. Liu, Y. Huang, X. Pu, J. Wang, F. Kang, J. Li, C. Xu, Few-layer $Ti_3C_2T_x$ MXene delaminated via flash freezing for high-rate electrochemical capacitive energy storage, *J. Energy Chem.* 48 (2020) 233–240, <https://doi.org/10.1016/j.jechem.2020.01.006>.
- [43] Z.H. Zeng, N. Wu, J.J. Wei, Y.F. Yang, T.T. Wu, B. Li, S.B. Hauser, W.D. Yang, J. R. Liu, S.Y. Zhao, Porous and ultra-flexible crosslinked MXene/polyimide composites for multifunctional electromagnetic interference shielding, *Nano-Micro Lett.* 14 (2022) 59, <https://doi.org/10.1007/s40820-022-00800-0>.
- [44] F. Shahzad, M. Alhabeb, C.B. Hatter, B. Anasori, S. Mai Hong, C.M. Koo, Y. Gogotsi, Electromagnetic interference shielding with 2D transition metal carbides (MXenes), *Science* 353 (2016) 1137–1140, <https://doi.org/10.1126/science.aag2421>.
- [45] Z. Zeng, M. Chen, H. Jin, W. Li, X. Xue, L. Zhou, Y. Pei, H. Zhang, Z. Zhang, Thin and flexible multi-walled carbon nanotube/waterborne polyurethane composites with high-performance electromagnetic interference shielding, *Carbon* 96 (2016) 768–777, <https://doi.org/10.1016/j.carbon.2015.10.004>.
- [46] M. Ma, Y. Liao, H. Lin, W. Shao, W. Tao, S. Chen, Y. Shi, H. He, Y. Zhu, X. Wang, Double-layer of CNF/rGO film and CNF/rGO/FeCo-LDO aerogel structured composites for efficient electromagnetic interference shielding, *Carbon* 220 (2024) 118863, <https://doi.org/10.1016/j.carbon.2024.118863>.
- [47] Q. Peng, M. Ma, Q. Chu, H. Lin, W. Tao, W. Shao, S. Chen, Y. Shi, H. He, X. Wang, Absorption-dominated electromagnetic interference shielding composite foam based on porous and bi-conductive network structures, *J. Mater. Chem. A* 11 (2023) 10857–10866, <https://doi.org/10.1039/D3TA01369C>.
- [48] A. Sotiropoulos, S. Koulouridis, A. Masouras, V. Kostopoulos, H.T. Anastassiou, Carbon nanotubes film in glass fiber polymer matrix forming structures with high absorption and shielding performance in X-band, *Compos. Pt. B-Eng.* 217 (2021) 108896, <https://doi.org/10.1016/j.compositesb.2021.108896>.
- [49] H. Fu, Y. Bai, S. Duan, H. Zhou, W. Gong, Structure design of multi-layered ABS/CNTs composite foams for EMI shielding application with low reflection and high absorption characteristics, *Appl. Surf. Sci.* 624 (2023) 157168, <https://doi.org/10.1016/j.apsusc.2023.157168>.
- [50] W. Cao, C. Ma, S. Tan, M. Ma, P. Wan, F. Chen, Ultrathin and flexible CNTs/MXene/cellulose nanofibrils composite paper for electromagnetic interference shielding, *Nano-Micro Lett.* 11 (2019) 72, <https://doi.org/10.1007/s40820-019-0304-y>.
- [51] G. Wang, D. Yi, X. Jia, J. Chen, B. Shen, W. Zheng, Structural design of compressible shape-memory foams for smart self-fixable electromagnetic shielding with reduced reflection, *Mater. Today Phys.* 22 (2022) 100612, <https://doi.org/10.1016/j.mtp.2022.100612>.
- [52] P. Yao, X. Li, Y. Zhang, K. Ma, X. Zhang, M. Li, J. Zuo, T. Li, L. Lin, C. Li, J. Xu, Electromagnetic wave absorption and shielding performances and mechanisms of a porous Ti_3AlC_2/SiC gradient composite, *ACS Appl. Electron. Mater.* 5 (2023) 1558–1565, <https://doi.org/10.1021/acsaelm.2c01595>.
- [53] Y. Yan, H. Xia, Y. Qiu, Z. Xu, Q.Q. Ni, Fabrication of gradient vapor grown carbon fiber based polyurethane foam for shape memory driven microwave shielding, *RSC Adv.* 9 (2019) 9401–9409, <https://doi.org/10.1039/C9RA00028C>.
- [54] Y. Guo, H. Qiu, K. Ruan, S. Wang, Y. Zhang, J. Gu, Flexible and insulating silicone rubber composites with sandwich structure for thermal management and electromagnetic interference shielding, *Compos. Sci. Technol.* 219 (2022) 109253, <https://doi.org/10.1016/j.compscitech.2021.109253>.
- [55] B. Wu, Y. Yu, K. Zhu, Y. Yang, X. Wen, R. Liu, H. Zhu, J. Huang, Efficient electromagnetic interference shielding of PPA6@NiM/PDMS composites with porous and asymmetric gradient structures, *ACS Appl. Polym. Mater.* 5 (2023) 4789–4798, <https://doi.org/10.1021/acsapm.3c00341>.
- [56] J. Xu, R. Chen, Z. Yun, Z. Bai, K. Li, S. Shi, J. Hou, X. Guo, X. Zhang, J. Chen, Lightweight epoxy/cotton fiber-based nanocomposites with carbon and Fe_3O_4 for electromagnetic interference shielding, *ACS Omega* 7 (2022) 15215–15222, <https://doi.org/10.1021/acsomega.2c01293>.
- [57] J. Zhang, D. Li, W. Zhu, Y. Li, In situ 3D printing of poly-ether-ether-ketone/poly-ether-imide hierarchical cellular foams containing electromagnetic absorbent, *Addit. Manuf.* 59 (2022) 103181, <https://doi.org/10.1016/j.addma.2022.103181>.
- [58] Y. Li, B. Shen, D. Yi, L. Zhang, W. Zhai, X. Wei, W. Zheng, The influence of gradient and sandwich configurations on the electromagnetic interference shielding performance of multilayered thermoplastic polyurethane/graphene composite foams, *Compos. Sci. Technol.* 138 (2017) 209–216, <https://doi.org/10.1016/j.compscitech.2016.12.002>.
- [59] A. Sheng, W. Ren, Y. Yang, D.X. Yan, H. Duan, G. Zhao, Y. Liu, Z.M. Li, Multilayer WPU conductive composites with controllable electro-magnetic gradient for absorption-dominated electromagnetic interference shielding, *Compos. Pt. A-Appl. Sci. Manuf.* 129 (2020) 105692, <https://doi.org/10.1016/j.compositesa.2019.105692>.
- [60] T. Li, G. Zhao, L. Zhang, G. Wang, B. Li, J. Gong, Ultralow-threshold and efficient EMI shielding PMMA/MWCNTs composite foams with segregated conductive network and gradient cells, *Express Polym. Lett.* 14 (2020) 685–703, <https://doi.org/10.3144/expresspolymlett.2020.56>.

- [61] H. Lin, X. Wang, L. Yu, Y. Chen, J. Shi, Two-dimensional ultrathin MXene ceramic nanosheets for photothermal conversion, *Nano Lett.* 17 (2017) 384–391, <https://doi.org/10.1021/acs.nanolett.6b04339>.
- [62] D. Xu, Z. Li, L. Li, J. Wang, Insights into the photothermal conversion of 2D MXene nanomaterials: synthesis, mechanism, and applications, *Adv. Funct. Mater.* 30 (2020) 2000712, <https://doi.org/10.1002/adfm.202000712>.
- [63] X. Liu, X. Jin, L. Li, J. Wang, Y. Yang, Y. Cao, W. Wang, Air-permeable, multifunctional, dual-energy-driven MXene-decorated polymeric textile-based wearable heaters with exceptional electrothermal and photothermal conversion performance, *J. Mater. Chem. A* 8 (2020) 12526–12537, <https://doi.org/10.1039/DOTA03048A>.